Impact of Background Dynamic and Thermodynamic States on Distinctive Annual Cycle of Near-Equatorial Tropical Cyclogenesis over the Western North Pacific

Liyuan DENG[1] and Tim LI[1,2*]

1 *Key Laboratory of Meteorological Disaster, Ministry of Education / Joint International Research Laboratory of Climate and Environmental Change / Collaborative Innovation Center on Forecast and Evaluation of Meteorological Disasters, Nanjing University of Information Science & Technology, Nanjing* 210044, *China*

2 *International Pacific Research Center and Department of Atmospheric Sciences, School of Ocean and Earth Science and Technology, University of Hawaii, Honolulu, HI* 96822, *USA*

(Received January 21, 2020; in final form March 24, 2020)

ABSTRACT

In a sharp contrast to tropical cyclone (TC) genesis over the main development region of the western North Pacific (WNP), near-equatorial (0°–5°N) TCs exhibit a distinctive annual cycle, peaking in boreal winter and being inactive in boreal summer. The relative roles of dynamic and thermodynamic background states on near-equatorial TCs formation were investigated based on the observational diagnosis of the genesis potential index (GPI) and high-resolution model simulations. It is found that the background vorticity makes a major contribution to the distinctive annual cycle, while mean temperature and specific humidity fields are not critical. Numerical simulations further indicate that seasonal mean cyclonic vorticity in boreal winter has three effects on TC genesis near the equator. First, the environmental cyclonic vorticity interacts with TC vortex to promote a mid-level outflow, which strengthens boundary layer friction induced ascending motion and thus condensational heating. Second, it produces an equivalent Coriolis effect (via enhanced absolute vorticity), which strengthens positive feedback between primary and secondary circulation. Third, it helps to merge small-scale vortical hot towers (VHTs) into a mesoscale core through vorticity segregation process. However, background vorticity in boreal summer has an opposite effect on TC development near the equator.

Key words: near-equatorial tropical cyclone (TC), equivalent Coriolis effect, vorticity segregation

Citation: Deng, L. Y., and T. Li, 2020: Impact of background dynamic and thermodynamic states on distinctive annual cycle of near-equatorial tropical cyclogenesis over the western North Pacific. *J. Meteor. Res.*, **34**(4), 822–835, doi: 10.1007/s13351-020-0007-9.

1. Introduction

Gray (1968) indicated that tropical cyclone (TC) genesis requires six necessary thermal and dynamic conditions, one of which is the Coriolis force. Many subsequent studies confirmed the importance of the planetary vorticity in TC formation as it is essential in connecting rotational and convergent flow (Anthes, 1982; Li et al., 2012). Therefore, it seemed logical to assume that TC genesis must occur a few latitude degrees away from the equator so that a region within 500 km north and south of the earth's equator should be TC-free. However, the current International Best Track for Climate Stewardship (IBTrACS) dataset (Knapp et al., 2010) reveals that during 1979–2018, 9 tropical storms (TSs) formed between 3°N and 3°S. In the western North Pacific (WNP) region, 76 TCs formed within 5°N during the same period.

Previous studies investigated some noteworthy near-equatorial typhoons (Fortner, 1958; Holliday and Thompson, 1986; McBride, 1995; Chang and Wong, 2008; Liu et al., 2010; Koseki et al., 2014). For instance, Fortner (1958) was the first to summarize the characteristics of near-equatorial Typhoon Sarah (1956) using the data from aerial weather reconnaissance. Holliday and

Supported by the National Natural Science Foundation of China (41630423 and 41875069), NOAA of U. S. (NA18OAR4310298), National Science Foundation of U. S. (AGS-1643297), China Scholarship Council (CSC; N201808320286), and Postgraduate Research and Practice Innovation Program of Jiangsu Province (KYCX18_1002).

*Corresponding author: timli@hawaii.edu.

©The Chinese Meteorological Society and Springer-Verlag Berlin Heidelberg 2020

Thompson (1986) noticed that the noteworthy near-equatorial Typhoon Kate (1970) was small enough to be in the micro-typhoon category. Its wind field was compact but intense, with maximum sustained winds of at least 54 m s^{-1}. Typhoon Vamei (2001) formed at 1.5°N on 26 December 2001 over the South China Sea and maintained its typhoon strength for 12 h (Chang et al., 2003; Chambers and Li, 2007; Juneng et al., 2007).

The WNP is the most active TC basin, because of the warmest sea surface temperature (SST) and favorable large-scale moisture and circulation conditions (Li, 2012; Li and Hsu, 2018). The analysis of annual cycle of nearly 40 yr near-equatorial typhoons and tropical storms (TSs) over the WNP showed that the most active (inactive) season is in boreal winter and early spring (boreal summer; Yi and Zhang, 2010; Li et al., 2019), which is in a great contrast to the seasonal variation of typhoons in the main development region of the WNP (i.e., monsoon trough) off the equator.

Given a weak Coriolis parameter near the equator, how could rotational flow interact with divergent flow? Previous studies suggested that the background relative vorticity may provide a favorable environment condition for near-equatorial TCs. For instance, Chang et al. (2003) pointed out that a strong and persistent cold surge in December 2001 provided a source for background cyclonic vorticity and was crucial for the genesis of Typhoon Vamei. Chambers and Li (2007) demonstrated that based on their numerical model experiments, the merging of small-scale vortices associated with vorticity segregation under a background cyclonic flow was critical for Vamei's development. Thus, the background mean vorticity may play a critical role in the formation of near-equatorial TCs.

So far, few studies focus on the seasonal variations of near-equatorial TC genesis and its dependence on large-scale background state. The goal of the current study is to understand the cause of the distinctive annual cycle of near-equatorial TCs and how the seasonal background mean states, in particular dynamic and thermodynamic mean fields, modulate the near-equatorial TC genesis. We will take a combined observational analysis and idealized numerical modeling approach. Dynamically, it is interesting to examine how near-equatorial TCs form under a weak planetary vorticity environment, as in this scenario, atmospheric rotational flow is weakly coupled with the divergent component of the wind.

The remaining of the paper is organized as follows. Section 2 presents a description of model configuration and experimental design. In Section 3, the relative roles of dynamic and thermodynamic seasonal mean fields in affecting near-equatorial TC development are investigated through both the observational analysis and sensitivity model experiments. Section 4 further reveals the critical processes that lead to the genesis and intensification of near-equatorial TCs. The conclusions and discussion are given in the last section.

2. Data and methods

2.1 *Data*

The WNP best-track data from the Joint Typhoon Warning Center (JTWC) were used to determine near-equatorial TC genesis cases and location. It is noted that all TCs studied here have a maximum intensity exceeding the TS strength (17.2 m s^{-1}). Thus, what we examined here is these tropical depressions that occurred initially in the near equatorial zone (< 5°N) but eventually developed into a TC.

The climatological mean states for each season are derived based on the NCEP Reanalysis 2 data (Kalnay et al., 1996) from 1979 to 2018, which has a horizontal resolution of 2.5° × 2.5° with 17 vertical pressure levels. The meteorological fields from the NCEP2 dataset including wind, temperature, geopotential height, relative humidity, surface pressure, and sea level pressure fields are used as initial and lateral boundary conditions in numerical model experiments.

2.2 *Model configuration*

A high-resolution mesoscale model, the Advanced Research Weather Research and Forecasting (WRF-ARW) version 3.7 (Hsiao et al., 2012), is used. The model is on the beta plane. The model is configured with two domains, a coarse mesh size of 610 × 510 and a finer mesh size of 300 × 300 with horizontal grid sizes of 9 and 3 km, respectively. The model consists of 27 vertical layers. The Kain–Fritch convective scheme is applied to the outer meshes (Kain and Fritsch, 1993), and an explicit microphysics scheme (Lin et al., 1983) is used in all meshes. The planetary boundary layer (PBL) turbulent closure scheme is adopted from the Yonsei University scheme (Hong et al., 2006) with an explicit entrainment layer and a parabolic K profile in unstable mixed layer. A fixed lateral boundary condition is used for the outer domain and the inner nested domains move automatically following the model vortex (Davis et al., 2008).

A weak axisymmetric vortex with a gradient wind balance is specified initially. The maximum tangential wind of the initial vortex is 15 m s^{-1} at the radius of 120 km at the surface. The initial vortex is placed in the center of the main analysis region.

2.3 *Experimental design*

Two control experiments were designed, one for the active season and the other for the inactive season, identified as W_CTL and S_CTL, respectively (Table 1). The experiment prefix of "W" or "S" denotes that the experiments are in the active season or the inactive season, respectively. The 40-yr averaged mean states of the two seasons including surface pressure, wind, geopotential height, temperature, SST, and specific humidity fields are used as initial and lateral boundary conditions. TC genesis could be triggered by various types of tropical perturbations including the Pacific easterly waves (Fu et al., 2007). It was pointed out that the energy accumulation of the easterly waves near the easterly and westerly confluence zone is a possible mechanism of TC formation (Kuo et al., 2001; Tam and Li, 2006). The energy source of the Pacific easterly waves is originated from midlatitude Pacific jet (Tam and Li, 2006). Another possible mechanism is the development of a precursory disturbance from an equatorial mixed Rossby-gravity wave (Dickinson and Molinari, 2002). In this study, however, we did not examine the precursory disturbances, but focus on the background mean state difference. The initial vortex in all experiments has the same structure and intensity.

Sensitivity experiments are designed to understand the relative roles of dynamic and thermodynamic environmental parameters on the near-equatorial TC genesis. Two sets of experiments are designed to examine the contributions of area-averaged vertical profiles of temperature (representing atmospheric static stability) and moisture. In the first set of experiments, we switch the temperature profiles between the active and inactive seasons. For example, the temperature profile in W_CTL was used in S_CTL, while other variables remain the same. This set of experiments is identified as W/S_change_T. Actually, in the sensitivity experiments when we change the area-averaged temperature vertical profile, the SST is also changed, as the air temperature near the surface is directly related to the underlying SST. The second set of experiments is to switch the specific humidity profile between the two seasons while keeping the other variables unchanged. This set of experiments is denoted as W/S_change_SH. It is worth mentioning that in all the sensitivity experiments, we only change the domain averaged vertical profiles of temperature or moisture so that the horizontally varying components are still in balance with the wind field. To examine the relative roles of atmospheric static stability and circulation fields, the temperature filed is separated into a domain averaged component and a perturbation component relative to the domain mean. The former is independent of the wind and is in the hydrostatic balance, whereas the latter is associated with the atmospheric wind field according to a thermal-wind relationship. Because the domain averaged temperature vertical profile is not related to the wind field, one may switch the vertical profiles of temperature from the active season to the inactive season. Similarly, we also separate the specific humidity field into the two components. Whereas the domain averaged moisture vertical profile may appear in a resting environment, the horizontal distribution of the moisture perturbation is often associated with the atmospheric motion through diabatic heating.

In summary, W_change_T (SH) and S_change_T (SH) have the same climate mean states as W_CTL and S_CTL except that the area-averaged temperature (specific humidity) profile in the opposite season is used. Two parallel runs were further conducted, one with an initial vortex and the other without an initial TC-like vortex. The difference between the two parallel runs would represent the "pure" vortex evolution as the specified initial background mean state evolves also with time as the model integrates forward. The control and sensitivity experiments are listed in Table 1.

2.4 *TC GPI*

Emanuel and Nolan (2004) developed a genesis poten-

Table 1. List of the control and sensitivity experiments

Group	Wind	Specific humidity	Temperature
W_CTL	Climatological mean wind in DJFMAM	Climatological mean specific humidity in DJFMAM	Climatological mean temperature in DJFMAM
S_CTL	Climatological mean wind in AS	Climatological mean specific humidity in AS	Climatological mean temperature in AS
W_change_T	Climatological mean wind in DJFMAM	Climatological mean specific humidity in DJFMAM	Area-averaged vertical temperature profile in AS
S_change_T	Climatological mean wind in AS	Climatological mean specific humidity in AS	Area-averaged vertical temperature profile in DJFMAM
W_change_SH	Climatological mean wind in DJFMAM	Area-averaged vertical specific humidity in AS	Climatological mean temperature in DJFMAM
S_change_SH	Climatological mean wind in AS	Area-averaged vertical specific humidity in DJFMAM	Climatological mean temperature in AS

Note: DJFMAM represents December–May (active season); AS represents August–September (inactive season).

tial index (GPI), which consists of four parameters, i.e., absolute vorticity, relative humidity, potential intensity, and vertical shear. In this study, we will use the GPI to measure how the environmental factors influence near-equatorial TC genesis. Following Li et al. (2013), the GPI may be written as

$$\mathrm{GPI} = T1 \times T2 \times T3 \times T4, \tag{1}$$

where $T1 = \left|10^5\eta\right|^{3/2}$, $T2 = (1 + 0.1V_{\mathrm{shear}})^{-2}$, $T3 = (H/50)^3$, and $T4 = (V_{\mathrm{P}}/70)^3$; η represents absolute vorticity at 850 hPa, V_{shear} represents the magnitude of vertical wind shear between 200 and 850 hPa, H is relative humidity at 600 hPa, and V_{P} represents the maximum potential intensity (MPI) defined by Emanuel (2000).

The derivative of the GPI formula was applied to quantitatively assess the relative contributions of the four environmental parameters to the GPI change. The change of GPI formula is written as follows:

$$\begin{aligned}\delta\mathrm{GPI} = {} & \delta T1 \times \overline{T2} \times \overline{T3} \times \overline{T4} + \delta T2 \times \overline{T1} \times \overline{T3} \times \overline{T4} \\ & + \delta T3 \times \overline{T1} \times \overline{T2} \times \overline{T4} + \delta T4 \times \overline{T1} \times \overline{T2} \times \overline{T3},\end{aligned} \tag{2}$$

where character " δ" represents a difference between the two analysis periods (active minus inactive season), and a bar denotes the climatological mean within the period. Through Eq. (2), one may investigate the relative contribution of individual terms to total GPI change.

3. Relative contributions of dynamic and thermodynamic fields

Figure 1 shows a sharp contrast between near-equatorial and off-equatorial TCs in the WNP. The TC genesis number is counted based on the initial position (first warning) of a TC in the best track data. Over the main TC development region in the WNP, maximum frequency occurs in boreal summer while minimum frequency occurs in boreal winter. TC genesis in the near-equatorial region is just opposite, with an active season in December–May (DJFMAM) and an inactive season from August to September (AS).

The climatological mean states for DJFMAM and AS are constructed by using the NCEP2 reanalysis data for the period of 1979–2018. Figure 2 shows the background vorticity, relative humidity, and wind fields at 850 hPa in the two seasons. The black dots denote the TC initial location. Cyclonic vorticity appears in the near-equatorial region in the active season, while anticyclonic vorticity appears in the inactive season.

Figure 3 illustrates the vertical profiles of area-averaged (black box in Fig. 2) relative vorticity and the differences of total wind speed, specific humidity, and temperature between the active and inactive seasons. Note that cyclonic vorticity appears throughout the troposphere during the active season, whereas anticyclonic vorticity dominates in the inactive season, with a maximum near 850 hPa (Fig. 3a). Figure 3b shows that the total wind speed is greater (smaller) near the surface (at 200 hPa) in the active season than in the inactive season. As a result, the vertical wind shear is smaller during the active season, which is more favorable for near-equatorial TC genesis. A warmer temperature in lower and middle troposphere and a cooler temperature in upper troposphere near the tropopause imply a more unstable stratification during the active season (Fig. 3d). The difference of specific humidity between the two seasons shows that a favorable moisture condition happens in the active season. A positive difference appears in lower troposphere, with a maximum magnitude (0.42 g kg^{-1}) at 925

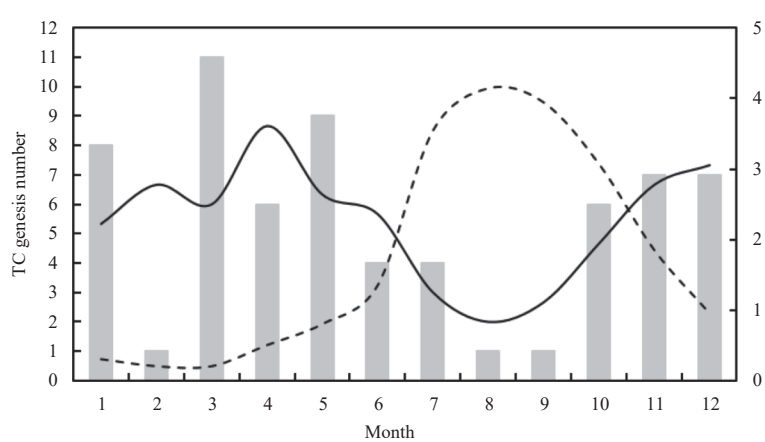

Fig. 1. Monthly evolutions of the total number mean (left y-axis; denoted by grey bars) and the 3-month running mean (left y-axis; denoted by the black solid line) of near-equatorial (< 5°N) TCs over the WNP, and the climatological monthly mean genesis number (right y-axis; denoted by the black dashed line) of TC over the main development region (5°–25°N, 120°–170°E) of the WNP during 1979–2018.

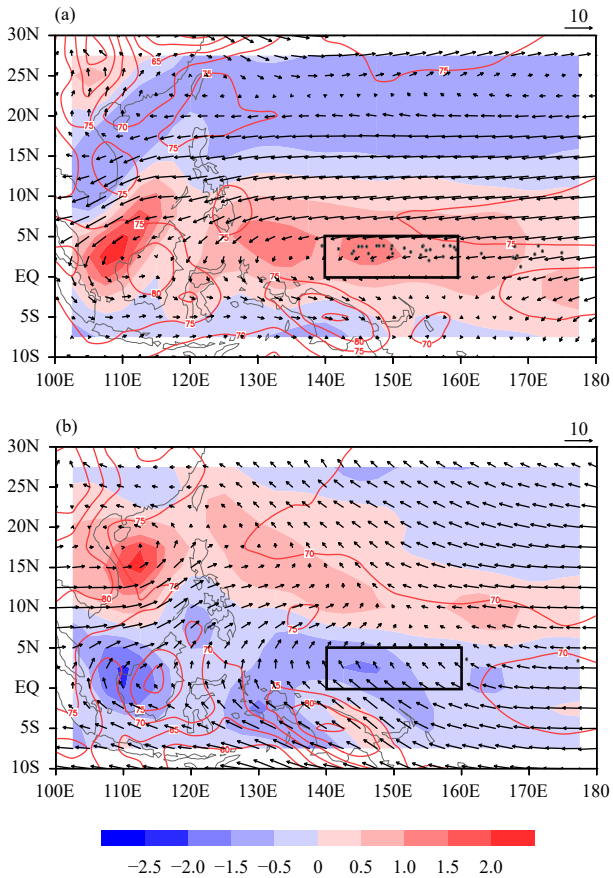

Fig. 2. The climatological background relative vorticity (shading; 10^{-5} s^{-1}), relative humidity (contours; %), and wind fields (vectors; m s^{-1}) at 850 hPa for the (a) active (DJFMAM) and (b) inactive (AS) seasons during 1979–2018. The black dots indicate the locations of near-equatorial (< 5°N) TCs during the same period.

hPa (Fig. 3c).

The vertical profile analysis above indicates that both the dynamic and thermodynamic states during the active season favor more TC formation frequency in the near-equatorial region. To understand their relative roles, we rely on the GPI analysis. Figure 4 shows the spatial distributions of GPI during the two periods and their difference (DJFMAM minus AS) field. In the active season, the GPI reaches its maximum over the near equatorial region (Fig. 4a). However, the maximum GPI center shifts greatly northward, with a maximum center around 18°N in August and September (Fig. 4b). The GPI difference map (Fig. 4c) shows a great contrast between the near- and off-equatorial region.

Given that the GPI is able to illustrate the TC genesis contrast between the near-equatorial and off-equatorial regions and between the active and inactive periods, we further investigate the relative contribution of each environmental parameter in the GPI formula, following Li et al. (2013). Figure 5 shows the diagnosis result for each term in Eq. (2). In the near-equatorial region (< 5°N), the absolute vorticity term is the major dominant term contributing to the seasonal difference of GPI. The vertical wind shear term also has a positive contribution. The relative humidity term and the MPI term, on the other hand, play a minor role in contributing to the seasonal contrast of the near-equatorial TCs.

The observational diagnosis result above is further confirmed by sensitivity model experiments. The goal of the numerical model experiments is to investigate the relative contributions of background dynamic (such as vorticity) and thermodynamic (such as vertical temperature and moisture profiles) mean states to near-equatorial TC genesis. All the sensitivity experiments are listed in Table 1.

Figure 6 compares the time evolutions of the minimum sea level pressure and the maximum wind speed for the following three sets of experiments: W/S_CTL, W/S_change_T, and W/S_change_SH. Note that in the W/S_change experiments, either the mean moisture or temperature vertical profiles have been changed. However, regardless of these changes, the initial vortex develops into a TC in all W-experiments, and fails to develop into a TC in all S-experiments. This implies that as long as the winter (summer) mean wind field is kept, an initial near-equatorial vortex will (will not) develop into a TC, regardless of what mean temperature and moisture profiles are given. Therefore, results from numerical model experiments indicate that the contribution of the background wind is most critical in causing the distinctive annual cycle of near-equatorial TCs. This confirms the observational diagnosis result.

4. Mechanisms for near-equatorial TC development

In this section, we investigate specific processes through which a TC forms under a low planetary vorticity environment. Because the specified mean flow also involves with time, to examine the "pure" vortex evolution, we re-run the W_CTL and S_CTL experiments without the initial vortex, and then subtract the original simulation results with the initial vortex from the new runs.

A key question addressed here is why the initial vortex could develop into a TC in W_CTL but failed in S_CTL. We first examine the structure differences during initial developing stage between the two experiments. Figure 7 shows the time evolutions of the vertical–radial cross-section of azimuthal-mean perturbation radial and tangential winds in the two experiments. While no signi-

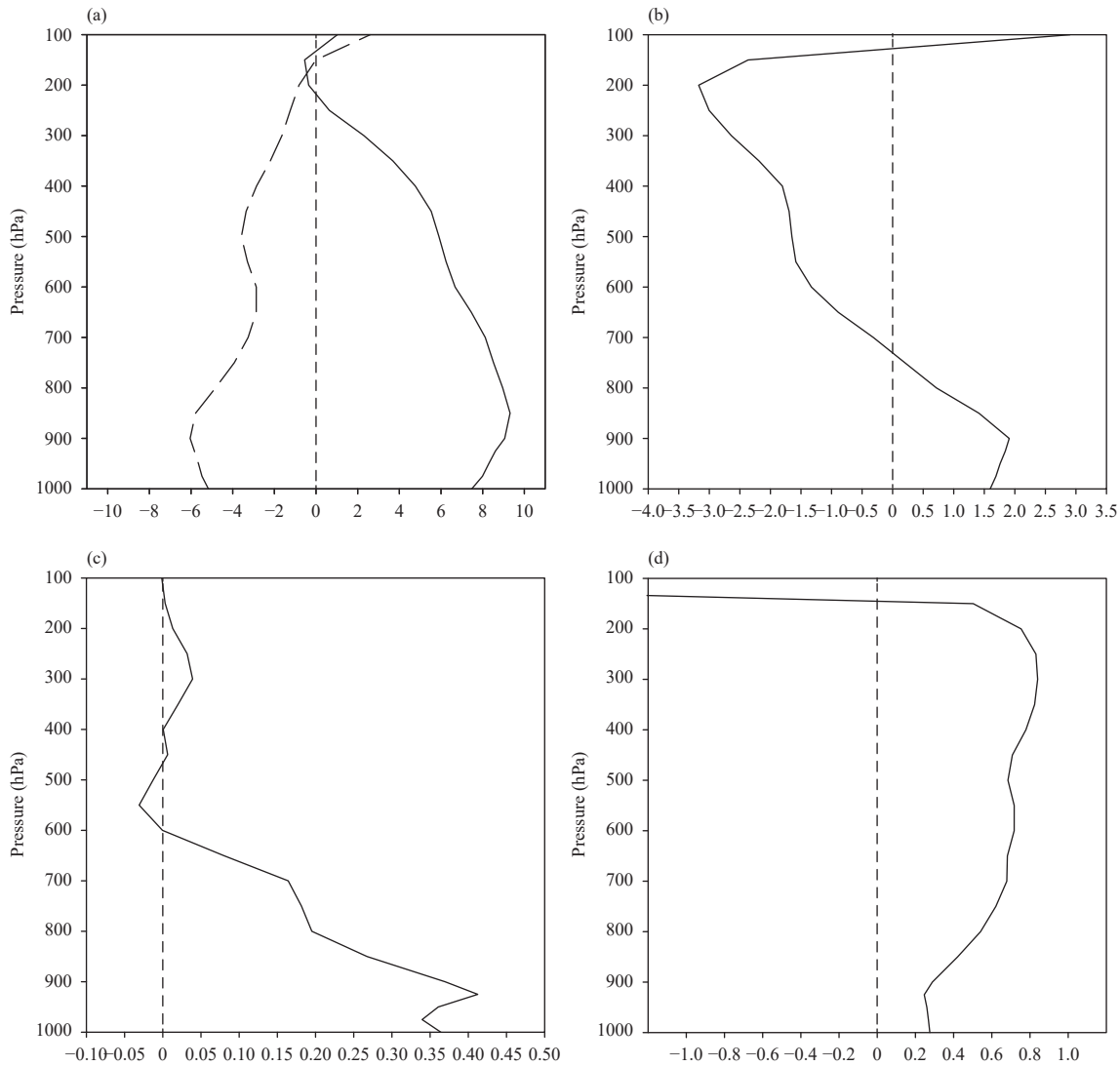

Fig. 3. Vertical profiles (the black box in Fig. 2) of the area-averaged (a) relative vorticity (10^{-6} s^{-1}) for the active (solid line) and inactive (long-dashed line) seasons, and the differences of the (b) total wind speed (m s^{-1}), (c) specific humidity (10^{-3} kg kg^{-1}), and (d) temperature (K) between the active and inactive seasons (DJFMAM minus AS) during 1979–2018. The vertical dashed line indicates the zero value of the respective parameter.

ficant difference occurs in the tangential wind field during hours 4–6 (Figs. 7a–f), the radial wind field does show a notable difference. A stronger inflow (outflow) appears in the boundary layer (middle troposphere) in W_CTL than in S_CTL (Figs. 7g–l). Based on the mass continuity, such a radial wind difference implies a distinctive vertical velocity profile between the two experiments.

Figure 8 shows the vertical–radial cross-sections of perturbation divergence and vertical motion during hours 4–6 in the two experiments. In W_CTL, strong divergence associated with the mid-level outflow appears throughout the free atmosphere (Figs. 8b–c). Accompanied by the deep-layer divergence is penetrated ascending motion throughout the troposphere (Figs. 8h–i). The greater ascending motion transports moisture upward, leading to a greater condensational heating (figure omitted). It is in a great contrast to S_CTL, in which maximum divergence associated with the outflow is confined below 2 km (Figs. 8e–f). As a result, a weak ascending center appears below 2 km (Fig. 8l).

Given that the only difference between the two experiments above is the specified mean state, the difference in the radial wind profile during the initial development stage arises from the mean flow interaction with the initial vortex. Following Cao et al. (2014), we diagnose the radial wind momentum budget. Decomposing total wind into the sum of vortex perturbation and background flow (i.e., $u = u' + \overline{u}$, where a prime denotes the perturbation and an overbar denotes the mean state), one may write a

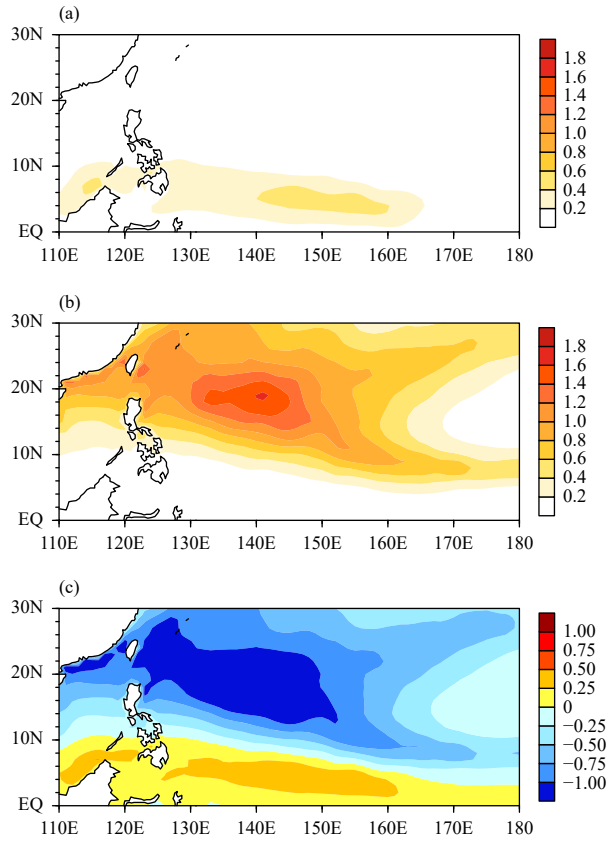

Fig. 4. Spatial patterns of the genesis potential index (GPI; shading) for the (a) active (DJFMAM) and (b) inactive (AS) seasons, and (c) the difference between them (DJFMAM minus AS) derived from NCEP2 reanalysis data during 1979–2018.

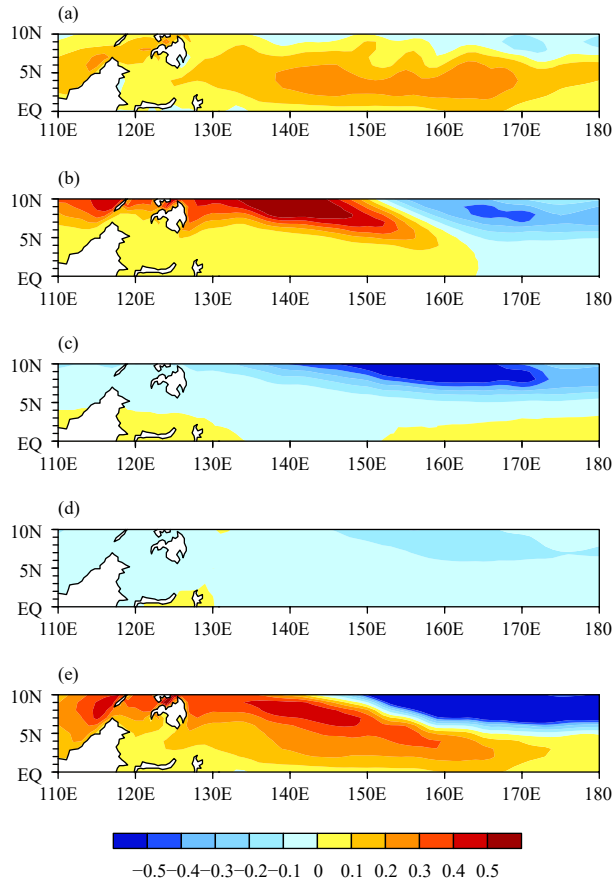

Fig. 5. Contributions of the four individual GPI changes: (a) term 1, (b) term 2, (c) term 3, and (d) term 4 to (e) the total GPI change in Eq. (2) between the active and inactive seasons (DJFMAM minus AS) during 1979–2018.

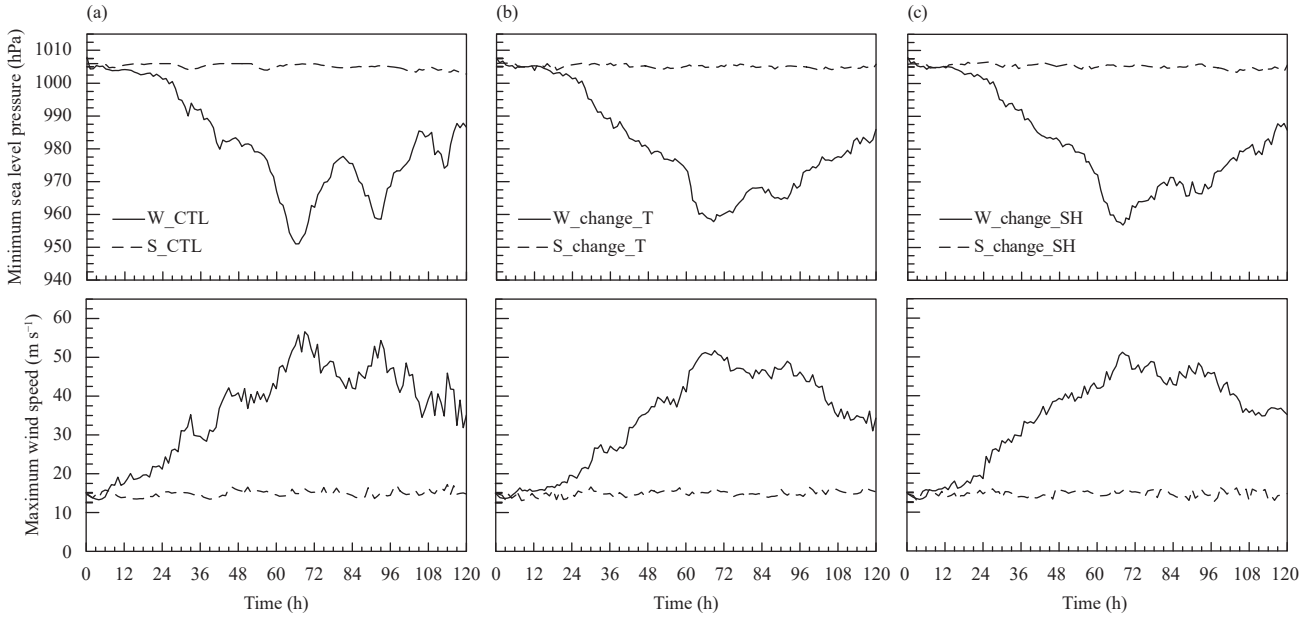

Fig. 6. Time evolutions of the minimum sea level pressure (upper panels; hPa) and the maximum tangential wind speed V_{max} (lower panels; m s^{-1}) in the control and sensitivity experiments: (a) W_CTL (solid line) and S_CTL (dashed line); (b) W_change_T (solid line) and S_change_T (dashed line); and (c) W_change_SH (solid line) and S_change_SH (dashed line).

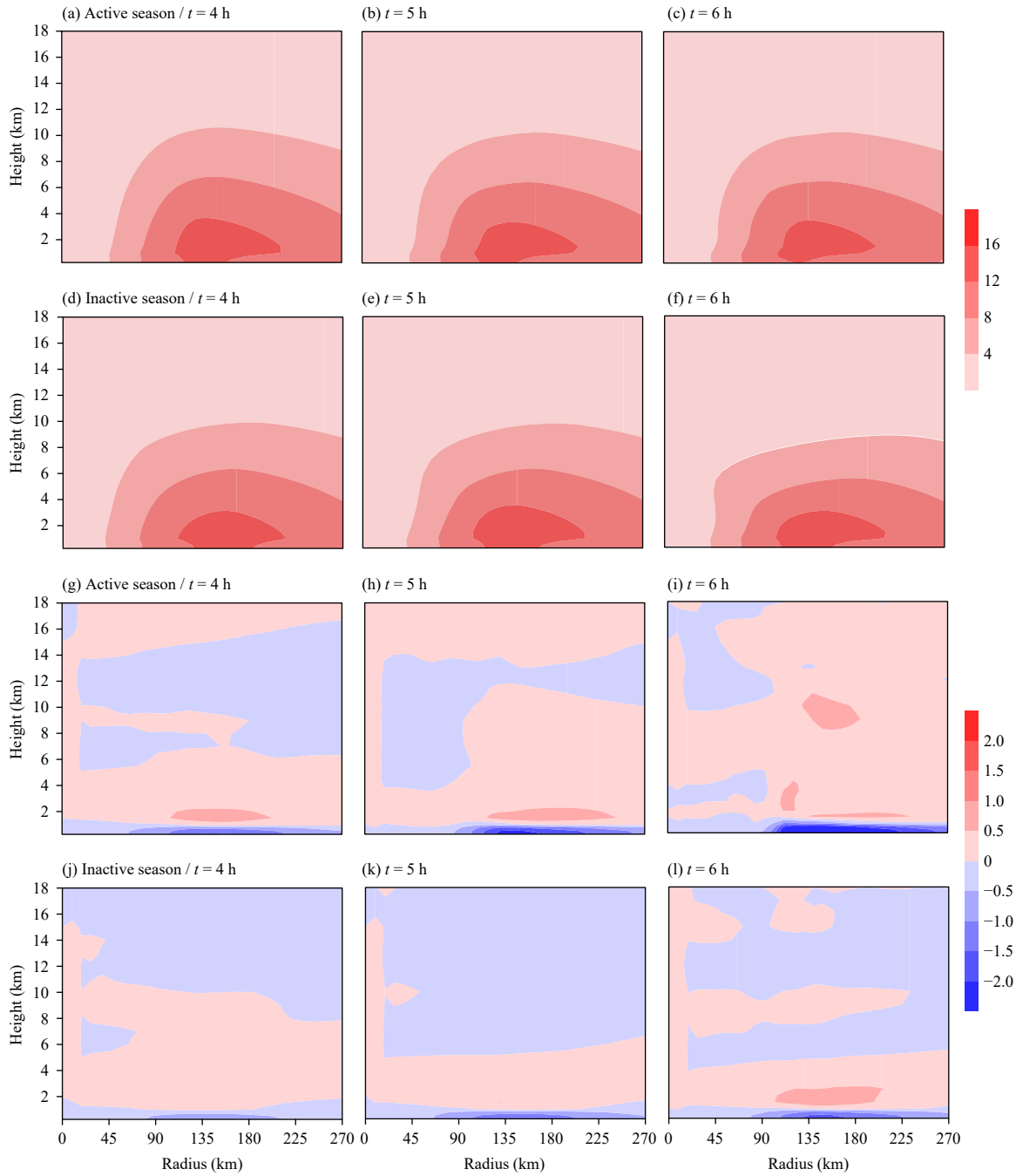

Fig. 7. Vertical–radial cross-sections of the azimuthal-mean (a–f) tangential wind (m s^{-1}) and (g–l) radial wind (m s^{-1}) in the (a–c, g–i) active and (d–f, j–l) inactive season simulations at (left panels) 4, (middle panels) 5, and (right panels) 6 h.

perturbation radial wind momentum equation as follows.

$$\frac{\partial u'}{\partial t} = -\left(\bar{u}\frac{\partial u'}{\partial r} + u'\frac{\partial \bar{u}}{\partial r} + u'\frac{\partial u'}{\partial r}\right) - \left(\frac{\bar{v}}{r}\frac{\partial u'}{\partial \lambda} + \frac{v'}{r}\frac{\partial \bar{u}}{\partial \lambda} + \frac{v'}{r}\frac{\partial u'}{\partial \lambda}\right) - \left(\bar{w}\frac{\partial u'}{\partial p} + w'\frac{\partial \bar{u}}{\partial p} + w'\frac{\partial u'}{\partial p}\right) + \left(f_0 v' + \frac{v'^2}{r}\right) + \frac{2v'\bar{v}}{r} - \frac{\partial \Phi'}{\partial r} + F'_u, \quad (3)$$

where λ is a azimuthal angle; r is radius; p is pressure; $\bar{u}$, $\bar{v}$, $\bar{w}$ are radial, tangential, and vertical wind speeds of the background flow, respectively; f_0 denotes the Coriolis parameter; u', v', w', and Φ' are radial, tangential, vertical winds, and the geopotential of the perturbation, respectively; and F'_u denotes horizontal and vertical diffusion. Since we specified the same initially symmetric vortex with gradient wind balance in the two experiments, the only tendency difference between the two experiments lies in the term $(2v'\bar{v}/r)$.

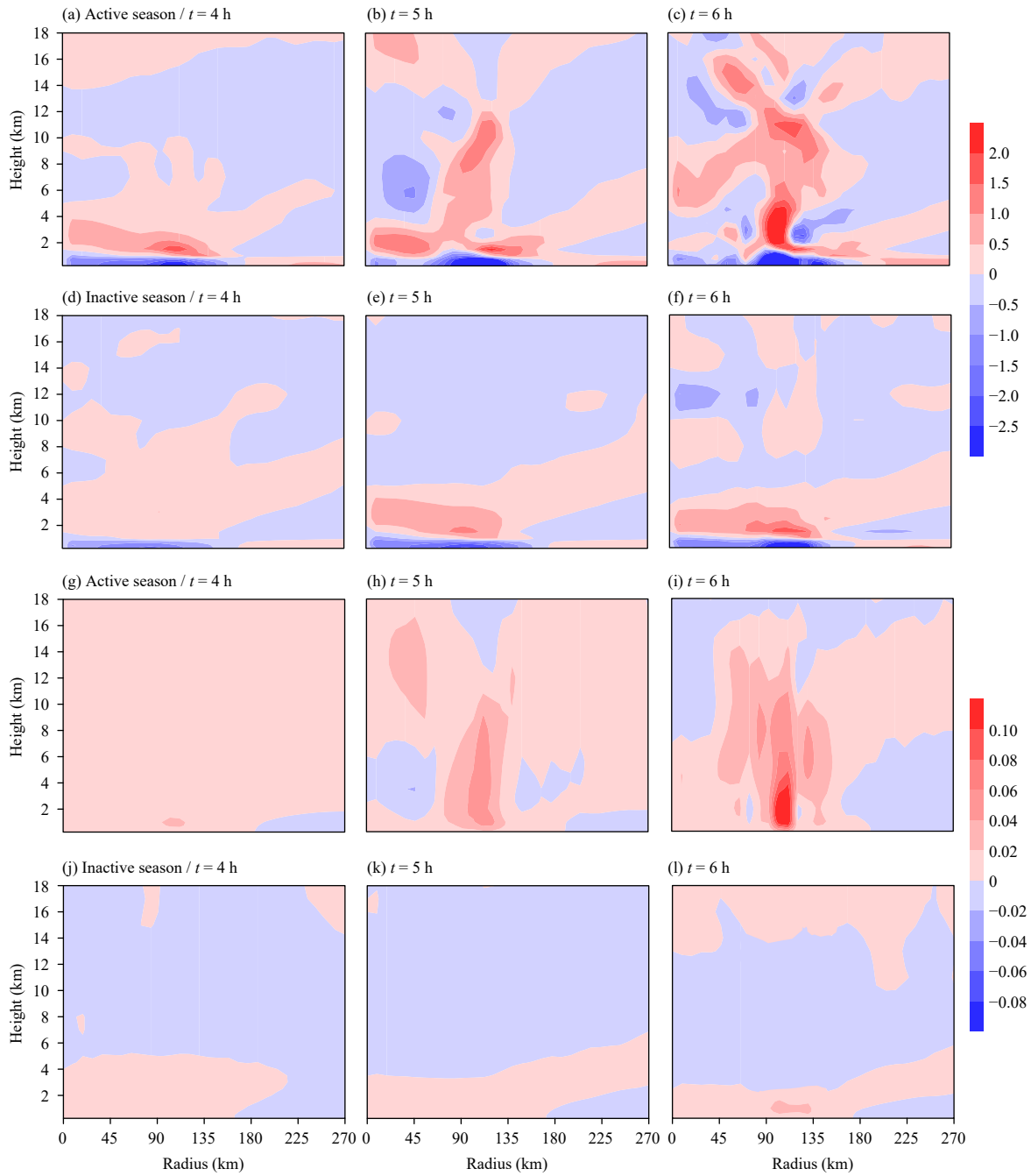

Fig. 8. As in Fig. 7, but for the azimuthal-mean (a–f) divergence (10^{-5} s^{-1}) and (g–l) vertical velocity (m s^{-1}) fields.

Figure 9 shows the vertical–radial distribution of this term at hour 4 in W_CTL and S_CTL. This term is mostly positive in middle troposphere in W_CTL as the mean state is of large-scale cyclonic circulation (Fig. 9a). It becomes negative in S_CTL because the mean state is of large-scale anticyclonic circulation (Fig. 9b). An enhanced mid-level outflow promotes ascending motion in the TC core region, which is conducive to the initial vortex development. A mid-level inflow, on the other hand, induces subsidence in the core region, which prohibits the development of ascending motion induced by boundary layer friction (Cao et al., 2014).

The right panel of Fig. 9 illustrates the time evolution of area-averaged (radius from 90 to 360 km and height from 2 to 4 km) term ($2v'\overline{v}/r$) in the two experiments. The term is always positive in W_CTL during a 60-h integration period. In the contrast, the term remains negative during the 60-h period in S_CTL.

Therefore, through the numerical model experiments above we learn that the first role of the background cyc-

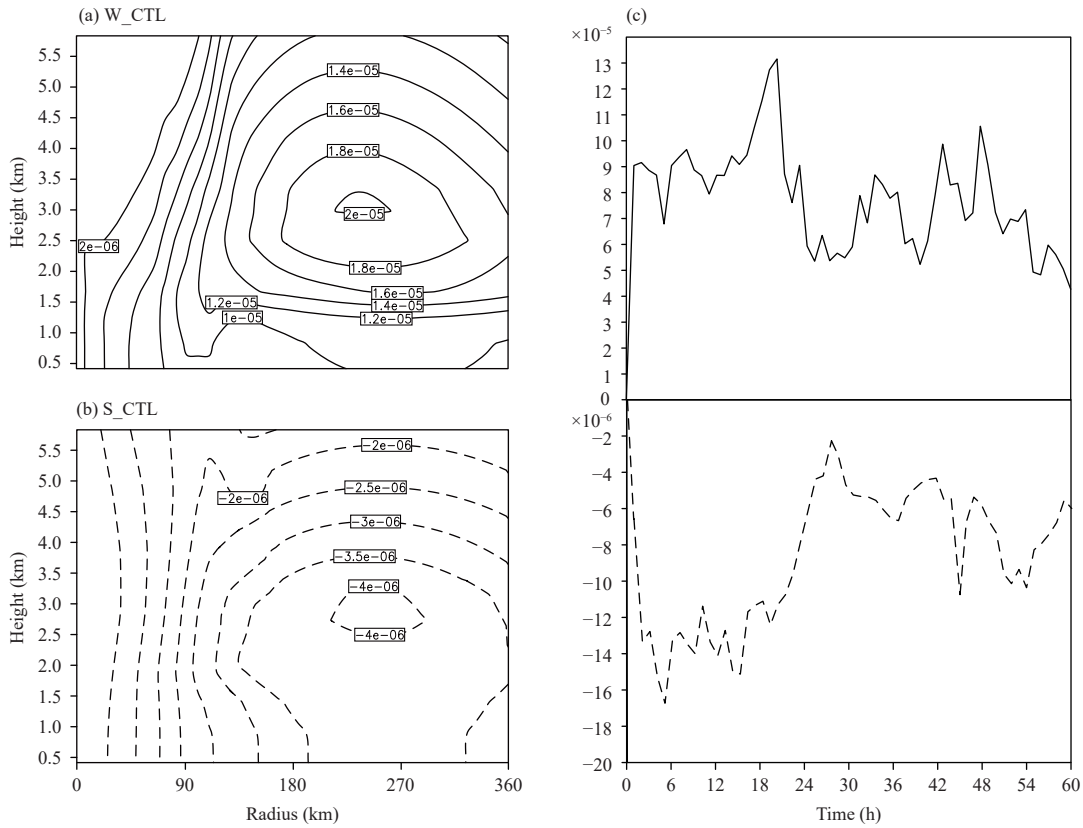

Fig. 9. Vertical–radial cross-sections of the azimuthal-mean term ($2v'\bar{v}/r$) (m s^{-2}) at t = 4 h in (a) W_CTL (solid lines) and (b) S_CTL (dashed lines). (c) Time evolutions of the area-averaged (radius: 90–360 km; height: 2–4 km) term ($2v'\bar{v}/r$) in W_CTL (solid line; upper panel) and S_CTL (dashed line; lower panel).

lonic vorticity is the modulation of mid-level radial wind. The second role is through a strengthened coupling between divergent and rotational wind components. In the lack of the mean flow, the relative vorticity equation in a pressure vertical coordinate under a constant f-plane, following Deng et al. (2018), may be written as

$$\frac{\partial \zeta}{\partial t} = -fD, \tag{4}$$

where ζ denotes relative vorticity, D denotes divergence, and f is the Coriolis parameter. Equation (4) indicates that a greater Coriolis parameter leads to a greater feedback from the divergent flow to the rotational flow (or from the secondary circulation to the primary circulation). Given the same low-level convergence, a greater TC intensification rate can be reached with a larger Coriolis parameter (Li et al., 2012; Deng et al., 2018). Near the equator, the Coriolis parameter becomes small, and as a result the positive feedback between primary and secondary circulation is weak. However, the background vorticity may act as an equivalent Coriolis force to strengthen the positive feedback. In the presence of the background mean vorticity, the relative vorticity equation may be written as:

$$\frac{\partial \zeta}{\partial t} = -(f + \zeta_{\mathrm{bg}}) \cdot D, \tag{5}$$

where ζ_{bg} denotes background vorticity. Therefore, the equivalent Coriolis effect tends to strengthen (weaken) the positive feedback when background relative vorticity is positive (negative). For the key TC genesis region (black box in Fig. 2), average latitude is around 3°N, and the corresponding planetary vorticity (f_{03}) is 7.6327×10^{-6} s^{-1}. The area-mean background relative vorticity in the region is about 10^{-5}s^{-1} in the active season and about −10^{-5} s^{-1} in the inactive season (Fig. 2). As a result, the equivalent Coriolis effect (i.e., sum of relative and planetary vorticity) is more than doubled during DJFMAM. This is equivalent to an increase of genesis latitude beyond 5°N. As discussed above, the strengthened Coriolis effect promotes a stronger positive feedback between the primary and secondary circulation. In a sharp contrast, the equivalent Coriolis effect becomes inefficient during the inactive season, prohibiting the positive feedback. As a result, the vortex fails to develop.

The third role of the background cyclonic vorticity is

that it tends to set up a mesoscale core through the merging of randomly generated small-scale vortical hot towers (VHTs; Li, 2012). Such a merging process is named as vorticity segregation (Schecter and Dubin, 1999). Figure 10 shows the time evolution of 850-hPa wind and potential vorticity (PV) fields from hours 0 to 36. It is clearly seen from Figs. 10a–d that small-scale PVs are first generated along the radius of maximum surface wind speed, because of enhanced surface evaporation and convective instability there. The small-scale PVs gradually merge towards the center of the vortex in W_CTL. However, such a merging is not clearly seen in S_CTL (Figs. 10e–h), even though initially small-scale PV development is similar.

The vorticity segregation (or axisymmetrization) is a key process for upscale cascade from cumulus-scale (–5 km) VHTs to a mesoscale core (with a radius around 50–100 km). Through this process, small-scale cyclonic (anticyclonic) vorticity anomalies move up (down) the environmental vorticity gradient (Montgomery et al., 2006; Tory et al., 2006). To better describe the structure and evolution characteristics of small-scale vorticity perturbations, we apply a spatial filter to the original vorticity field to retain only the wavelength smaller than 100 km. Figure 11 illustrates the evolutions of horizontal patterns of the filtered 850-hPa relative vorticity anomalies. In W_CTL, after small-scale vorticity anomalies develop initially along the radius of maximum wind, they move toward the vortex center. However, in S_CTL, they tend to move away from the vortex center and dissipate under a large-scale anticyclone environment. Thus, the presence of the background cyclonic vorticity during the active season is critical in organizing small-scale VHTs and in the establishment of a mesoscale core. Once reaching this state, TC enters a self-sustained development stage, which is signified by a rapid drop of minimum sea level pressure (Li, 2012; Ge et al., 2013).

5. Conclusions and discussion

TCs near the equator (< 5°N) exhibit a distinctive annual cycle with a peak (inactive) season in DJFMAM (AS). This is opposite to TCs in the main development region of the WNP. The cause of this distinctive annual cycle was investigated through both the observational analysis and idealized numerical model experiments.

The diagnosis of the GPI indicates that this index is able to capture the distinctive annual cycle of near-equatorial TCs. A further separation of individual terms suggests that the major cause of the distinctive seasonal vari-

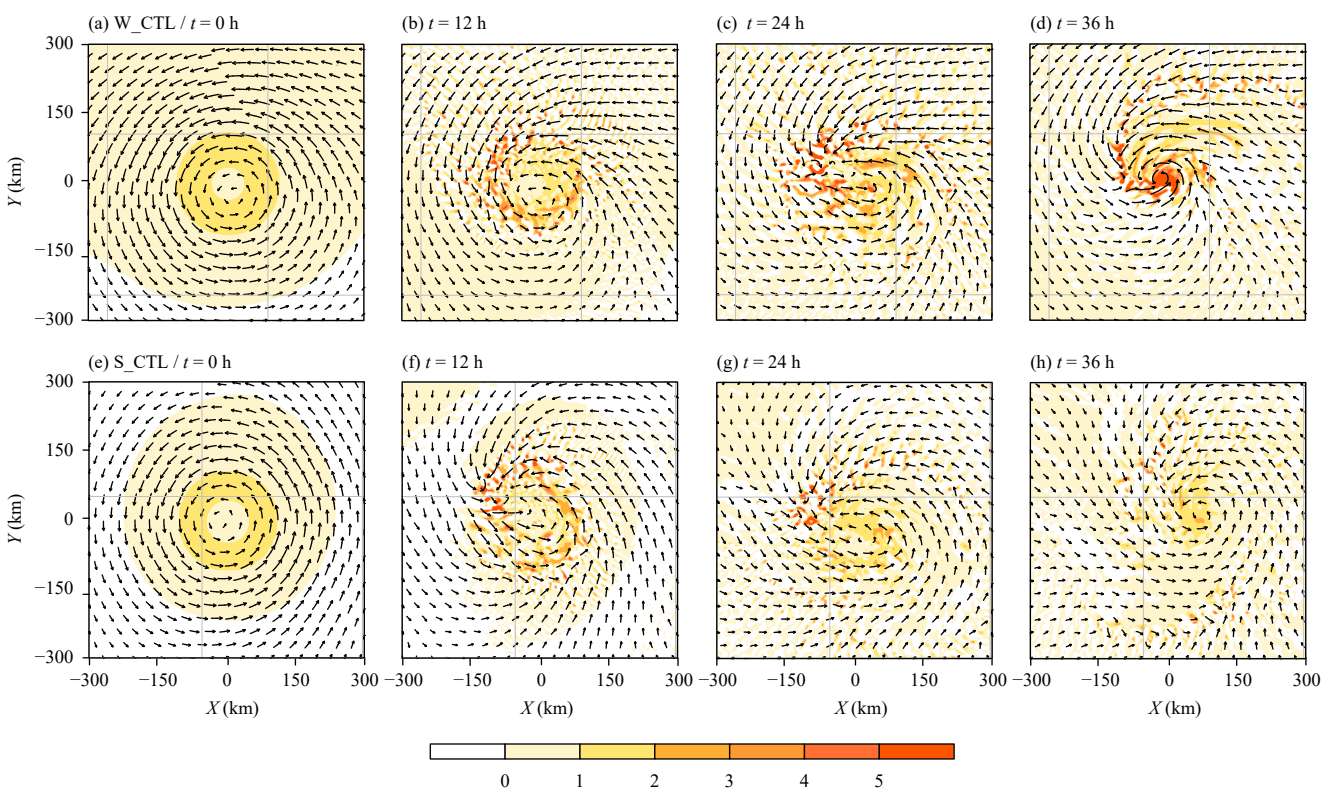

Fig. 10. Time evolutions of the potential vorticity (PV; shading; 10^{-6} K m^2 kg^{-1} s^{-1}) and wind (vectors; m s^{-1}) fields at 850 hPa in (a)–(d) W_CTL and (e)–(h) S_CTL at 0, 12, 24, and 36 h.

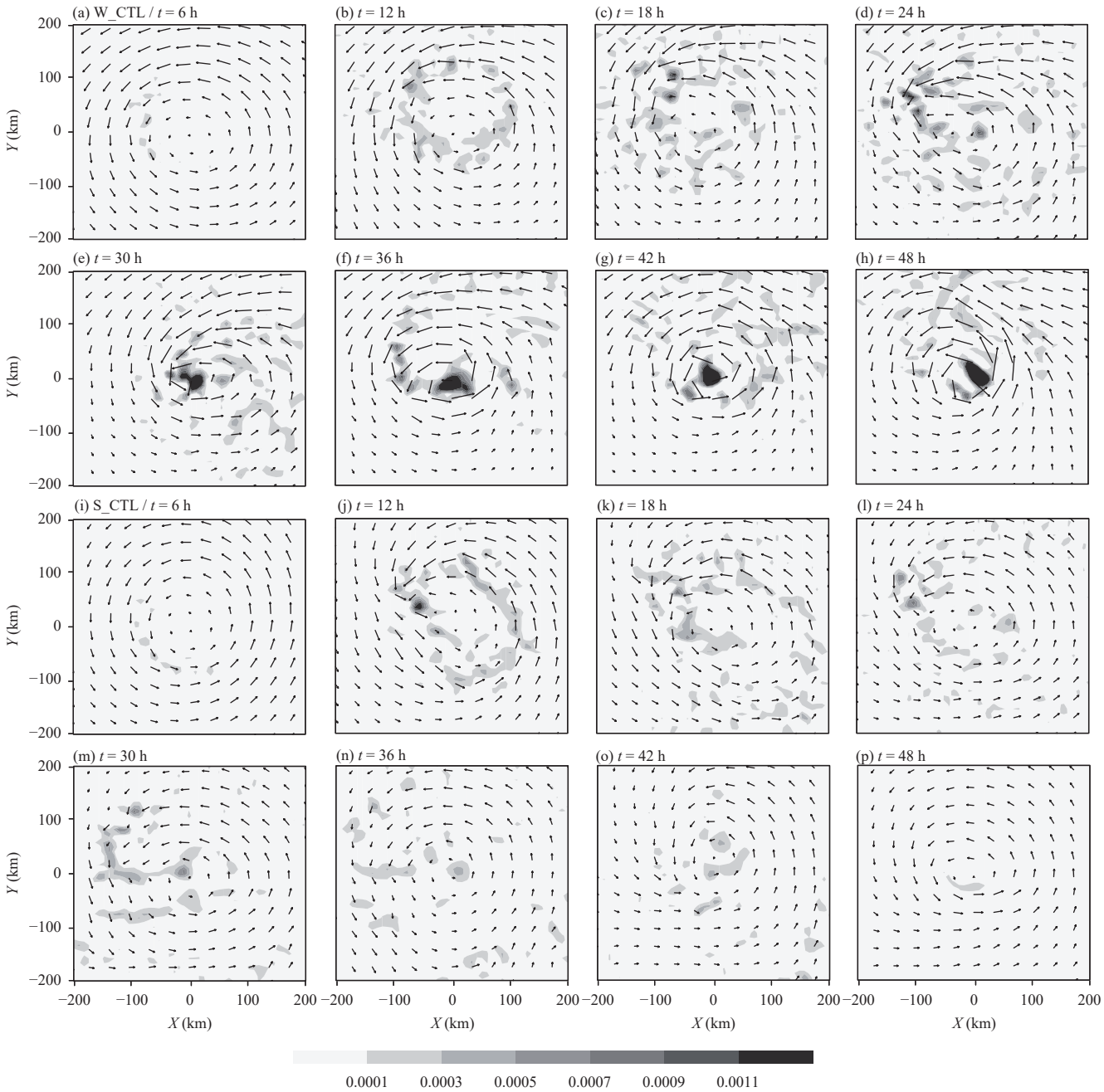

Fig. 11. Horizontal patterns of the filtered (with wavelength < 100 km) relative vorticity anomaly (shading; s^{-1}) and wind (vectors; m s^{-1}) fields at 850 hPa in (a–h) W_CTL and (i–p) S_CTL at 6, 12, 18, 24, 30, 36, 42, and 48 h.

ability lies in background low-level vorticity. Other environmental factors such as specific humidity and temperature are not important.

The control model experiments with specific mean states in the active and inactive seasons further confirm the mean state effect. The relative roles of dynamic and thermodynamic fields of the mean state in regulating TC genesis near the equator were further investigated through two sets of sensitivity experiments. The numerical results indicate that the background circulation is critical for the seasonal TC frequency change, while the annual cycle of the background temperature and moisture is not essential.

The diagnosis of the model simulations points out three mechanisms through which background vorticity affects near-equatorial TC genesis. First, it is through an interaction with TC vortex. The interaction leads to mid-level outflow in the presence of cyclonic environmental vorticity during DJFMAM. The outflow helps accelerate friction induced ascending motion, which strengthens up-

ward moisture transport and condensational heating. However, a mid-level inflow is generated in the presence of anticyclonic environmental vorticity during AS, which suppresses friction induced ascending motion and prohibits vortex development.

Second, the background vorticity affects near-equatorial TC genesis through an equivalent Coriolis effect. A positive environmental vorticity during the active season helps strengthen the positive feedback between the secondary and primary circulation and thus vortex development, which is equivalent to increasing the genesis latitude. On the other hand, a negative environmental vorticity prohibits the positive feedback so that the vortex fails to grow.

Third, the background vorticity greatly modulates the small-scale VHTs merging. Our numerical model experiments demonstrate that in the presence of a large-scale background cyclonic vorticity, small-scale convective cells or VHTs move towards the environmental vorticity center, through the vorticity segregation process. The merging eventually leads to the establishment of a mesoscale core at the characteristic scale of 50–100 km. This upscale cascade is critical for vortex development. In the contrast, the convective cells move away from the vortex center in the presence of an anticyclonic vorticity environment during the inactive season, which leads to a failure of TC formation.

An interesting question is why a cyclonic (anticyclonic) vorticity appears in the region of interest in DJFMAM (AS), which is opposite to the main development region. We speculate that it is attributed to the seasonal shift of the inter-tropical convergence zone (ITCZ) and the Coriolis force. In boreal winter, maximum cyclonic vorticity appears around 5°N because of the curvature of southward cross-equatorial flow. The occurrence of the near-equatorial cyclonic vorticity zone is accompanied by the southward shift of the subtropical high in the Northern Hemispheric winter. In contrast, in boreal summer the curvature of northward cross-equatorial flow due to the Coriolis force leads to an anticyclonic vorticity zone in the near-equatorial WNP, as the ITCZ and monsoon trough appear around 10°–20°N (Fig. 2b). Further studies are needed to understand the cause of the seasonal mean state change near the equator.

REFERENCES

Anthes, R. A., 1982: *Tropical Cyclones: Their Evolution, Structure and Effects*. American Meteorological Society, Boston, MA, 208 pp, doi: 10.1007/978-1-935704-28-7.

Cao, X., T. Li, M. Peng, et al., 2014: Effects of monsoon trough intraseasonal oscillation on tropical cyclogenesis over the western North Pacific. *J. Atmos. Sci.*, **71**, 4639–4660, doi: 10.1175/JAS-D-13-0407.1.

Chambers, C. R. S., and T. Li, 2007: Simulation of formation of a near-equatorial typhoon Vamei (2001). *Meteor. Atmos. Phys.*, **98**, 67–80, doi: 10.1007/s00703-006-0229-0.

Chang, C. P., and T. S. Wong, 2008: Rare typhoon development near the equator. *Recent Progress in Atmospheric Sciences: Applications to the Asia–Pacific Region*, K. N. Liou, M. D. Chou, and H. H. Hsu, Eds., World Scientific, Singapore, 172–181, doi: 10.1142/9789812818911_0010.

Chang, C. P., C. H. Liu, and H. C. Kuo, 2003: Typhoon Vamei: An equatorial tropical cyclone formation. *Geophys. Res. Lett.*, **30**, 1150, doi: 10.1029/2002GL016365.

Davis, C., W. Wang, S. S. Chen, et al., 2008: Prediction of landfalling hurricanes with the Advanced Hurricane WRF model. *Mon. Wea. Rev.*, **136**, 1990–2005, doi: 10.1175/2007MWR2085.1.

Deng, L. Y., T. Li, M. Y. Bi, et al., 2018: Dependence of tropical cyclone development on Coriolis parameter: A theoretical model. *Dyn. Atmos. Oceans*, **81**, 51–62, doi: 10.1016/j.dynatmoce.2017.12.001.

Dickinson, M., and J. Molinari, 2002: Mixed Rossby–gravity waves and western Pacific tropical cyclogenesis. Part I: Synoptic evolution. *J. Atmos. Sci.*, **59**, 2183–2196, doi: 10.1175/1520-0469(2002)059<2183:MRGWAW>2.0.CO;2.

Emanuel, K. A., 2000: A statistical analysis of tropical cyclone intensity. *Mon. Wea. Rev.*, **128**, 1139–1152, doi: 10.1175/1520-0493(2000)128<1139:asaotc>2.0.co;2.

Emanuel, K. A., and D. S. Nolan, 2004: Tropical cyclone activity and the global climate system. Proceedings of the 26th Conference on Hurricanes and Tropical Meteorology, Miami, FL, American Meteorological Society, 240–241.

Fortner Jr, C. L. E., 1958: Typhoon Sarah, 1956. *Bull. Amer. Meteor. Soc.*, **39**, 633–639, doi: 10.1175/1520-0477-39.12.633.

Fu, B., T. Li, M. S. Peng, et al., 2007: Analysis of tropical cyclogenesis in the western North Pacific for 2000 and 2001. *Wea. Forecasting*, **22**, 763–780, doi: 10.1175/waf1013.1.

Ge, X. Y., T. Li, and M. S. Peng, 2013: Tropical cyclone genesis efficiency: Mid-level versus bottom vortex. *J. Trop. Meteor.*, **19**, 197–213, doi: 10.1175/JCLI-D-12-00548.1.

Gray, W. M., 1968: Global view of the origin of tropical disturbances and storms. *Mon. Wea. Rev.*, **96**, 669–700, doi: 10.1175/1520-0493(1968)096<0669:GVOTOO>2.0.CO;2.

Holliday, C. R., and A. H. Thompson, 1986: An unusual near-equatorial typhoon. *Mon. Wea. Rev.*, **114**, 2674–2677, doi: 10.1175/1520-0493(1986)114<2674:AUNET>2.0.CO;2.

Hong, S.-Y., Y. Noh, and J. Dudhia, 2006: A new vertical diffusion package with an explicit treatment of entrainment processes. *Mon. Wea. Rev.*, **134**, 2318–2341, doi: 10.1175/MWR3199.1.

Hsiao, L. F., D. S. Chen, Y. H. Kuo, et al., 2012: Application of WRF 3DVAR to operational typhoon prediction in Taiwan: Impact of outer loop and partial cycling approaches. *Wea. Forecasting*, **27**, 1249–1263, doi: 10.1175/WAF-D-11-00131.1.

Juneng, L., F. T. Tangang, C. J. C. Reason, et al., 2007: Simulation of tropical cyclone Vamei (2001) using the PSU/NCAR MM5 model. *Meteor. Atmos. Phys.*, **97**, 273–290, doi: 10.1007/s00703-007-0259-2.

Kain, J. S., and J. M. Fritsch, 1993: Convective parameterization for mesoscale models: The Kain–Fritsch scheme. *The Representation of Cumulus Convection in Numerical Models*, K. A. Emanuel, and D. J. Raymond, Eds., American Meteorological Society, Boston, MA, 165–170, doi: 10.1007/978-1-935704-13-3_16.

Kalnay, E., M. Kanamitsu, R. Kistler, et al., 1996: The NCEP/NCAR 40-year reanalysis project. *Bull. Amer. Meteor. Soc.*, **77**, 437–471, doi: 10.1175/1520-0477(1996)077<0437:TNYRP>2.0.CO;2.

Knapp, K. R., M. C. Kruk, D. H. Levinson, et al., 2010: The international best track archive for climate stewardship (IBTrACS): Unifying tropical cyclone data. *Bull. Amer. Meteor. Soc.*, **91**, 363–376, doi: 10.1175/2009BAMS2755.1.

Koseki, S., T. Y. Koh, and C. K. Teo, 2014: Borneo vortex and mesoscale convective rainfall. *Atmos. Chem. Phys.*, **14**, 4539–4562, doi: 10.5194/acp-14-4539-2014.

Kuo, H.-C., J.-H. Chen, R. T. Williams, et al., 2001: Rossby waves in zonally opposing mean flow: Behavior in Northwest Pacific summer monsoon. *J. Atmos. Sci.*, **58**, 1035–1050, doi: 10.1175/1520-0469(2001)058<1035:rwizom>2.0.co;2.

Li, T., 2012: Synoptic and climatic aspects of tropical cyclogenesis in western North Pacific. *Cyclones: Formation, Triggers and Control*, K. Oouchi, and H. Fudeyasu, Eds., Nova Science Publishers, Inc, Hauppauge, 61–94.

Li, T., and P. C. Hsu, 2018: Tropical cyclone formation. *Fundamentals of Tropical Climate Dynamics*, T. Li, and P. C. Hsu, Eds., Springer, Cham, 107–147, doi: 10.1007/978-3-319-59597-9_4.

Li, T., X. Y. Ge, M. Peng, et al., 2012: Dependence of tropical cyclone intensification on the Coriolis parameter. *Tropical Cyclone Research and Review*, **1**, 242–253, doi: 10.6057/2012TCRR02.04.

Li, Y., T. Li, C. F. Fu, et al., 2019: Near-equatorial tropical cyclone formation in western North Pacific: Peak season and controlling parameter. *Climate Dyn.*, **52**, 2765–2773, doi: 10.1007/s00382-018-4291-3.

Li, Z., W. D. Yu, T. Li, et al., 2013: Bimodal character of cyclone climatology in the Bay of Bengal modulated by monsoon seasonal cycle. *J. Climate*, **26**, 1033–1046, doi: 10.1175/jcli-d-11-00627.1.

Lin, Y. L., R. D. Farley, and H. D. Orville, 1983: Bulk parameterization of the snow field in a cloud model. *J. Climate Appl. Meteor.*, **22**, 1065–1092, doi: 10.1175/1520-0450(1983)022<1065:BPOTSF>2.0.CO;2.

Liu, G. R., C. C. Liu, C. S. Huang, et al., 2010: Diagnosing the growth of equatorial Typhoon Vamei (2001) from an energy standpoint. *Terr. Atmos. Ocean Sci.*, **21**, 817–827, doi: 10.3319/TAO.2009.12.03.01(A).

McBride, J. L., 1995: Tropical cyclone formation. *Global Perspectives on Tropical Cyclone*, R. L. Elsberry, Ed., World Meteorological Organization, Geneva, Switzerland, 63–105.

Montgomery, M. T., M. E. Nicholls, T. A. Cram, et al., 2006: A vortical hot tower route to tropical cyclogenesis. *J. Atmos. Sci.*, **63**, 355–386, doi: 10.1175/jas3604.1.

Schecter, D. A., and D. H. E. Dubin, 1999: Vortex motion driven by a background vorticity gradient. *Phys. Rev. Lett.*, **83**, 2191–2194, doi: 10.1103/PhysRevLett.83.2191.

Tam, C.-Y. and T. Li, 2006: The origin and dispersion characteristics of the observed tropical summertime synoptic-scale waves over the western Pacific. *Mon. Wea. Rev.*, **134**, 1630–1646, doi: 10.1175/mwr3147.1.

Tory, K. J., M. T. Montgomery, and N. E. Davidson, 2006: Prediction and diagnosis of tropical cyclone formation in an NWP system. Part I: The critical role of vortex enhancement in deep convection. *J. Atmos. Sci.*, **63**, 3077–3090, doi: 10.1175/JAS3764.1.

Yi, B. Q., and Q. H. Zhang, 2010: Near-equatorial typhoon development: Climatology and numerical simulations. *Adv. Atmos. Sci.*, **27**, 1014–1024, doi: 10.1007/s00376-009-9033-3.